

3D Bivariate Spatial Modelling of Argo Ocean Temperature and Salinity Profiles

Mary Lai O. Salvaña and Mikyoung Jun¹

October 24, 2022

Abstract

Variables contained within the global oceans can detect and reveal the effects of the warming climate as the oceans absorb huge amounts of solar energy. Hence, information regarding the joint spatial distribution of ocean variables is critical for climate monitoring. In this paper, we investigate the spatial correlation structure between ocean temperature and salinity using data harvested from the Argo program and construct a model to capture their bivariate spatial dependence from the surface to the ocean's interior. We develop a flexible class of multivariate nonstationary covariance models defined in 3-dimensional (3D) space (longitude \times latitude \times depth) that allows for the variances and correlation to change along the vertical pressure dimension. These models are able to describe the joint spatial distribution of the two variables while incorporating the underlying vertical structure of the ocean. We demonstrate that proposed cross-covariance models describe the complex vertical cross-covariance structure well, while existing cross-covariance models including bivariate Matérn models poorly fit empirical cross-covariance structure. Furthermore, the results show that using one more variable significantly enhances the prediction of the other variable and that the estimated spatial dependence structures are consistent with the ocean stratification.

Some key words: 3D covariance functions; Argo; cross-covariance function; nonstationary; salinity; spatial; temperature.

¹Department of Mathematics, University of Houston, 4800 Calhoun Rd, Houston, TX 77004, USA
E-mail: msalvana@central.uh.edu mjun@central.uh.edu.

Mikyoung Jun acknowledges support by NSF DMS-1925119 and DMS-2123247. The authors also acknowledge helpful discussions with Mikael Kuusela on Argo data.

1 Introduction

The international scientific program named Array for Real-time Geostrophic Oceanography (ARGO) was launched in the early 2000s as a response to the call of global observation networks to monitor the climate system (Argo, 2000; Johnson et al., 2022). Since then, the program has launched a global network of 4000 free-drifting Argo profiling floats that measure ocean variables in the upper 2000 meters of the world’s oceans. Each float performs a ten day duration “park-and-profile” mission. From the surface, the float descends to the drift depth at 1000 meters where it will park for 9 days. At the 10th day, the float descends to 2000 meters and collects temperature (in degree Celsius or °C), salinity (in practical salinity unit or PSU), and pressure (in decibars or dbar) measurements as it ascends to the surface. Once at the surface, the data collected are transmitted via satellite. The full “park-and-profile” mission is illustrated in Figure 1. The data harvested by the floats are made available within 24 hours of its collection as Argo data products (<https://argo.ucsd.edu>). By making the data publicly accessible, the Argo program offers the research community the opportunity to analyze ocean processes and challenges modelers to improve existing data-driven scientific methods.

The core Argo data products are temperature and salinity measurements, the two most important variables through which other oceanographic variables, such as freezing point, electrical conductivity, viscosity (Pawlowicz, 2013), ocean heat content and potential density (Yarger et al., 2022), and tropical cyclone-induced ocean thermal response (Hu et al., 2020), can be derived. The temperature and salinity variables have been key pieces in understanding the physical properties and dynamics of the ocean. Their distributions were shown to drive ocean circulation (Chen et al., 2022; Gangopadhyay, 2022), affect climate processes (Olson et al., 2022), and change biogeochemistry (Galán et al., 2021; Ding et al., 2022). They were also used to understand underwater sound propagation for hydroacoustics research (Jana et al., 2022), design offshore wind farms (Escobar et al., 2016), and identify stressors to organisms in seawater and freshwater (Walker et al., 2020).

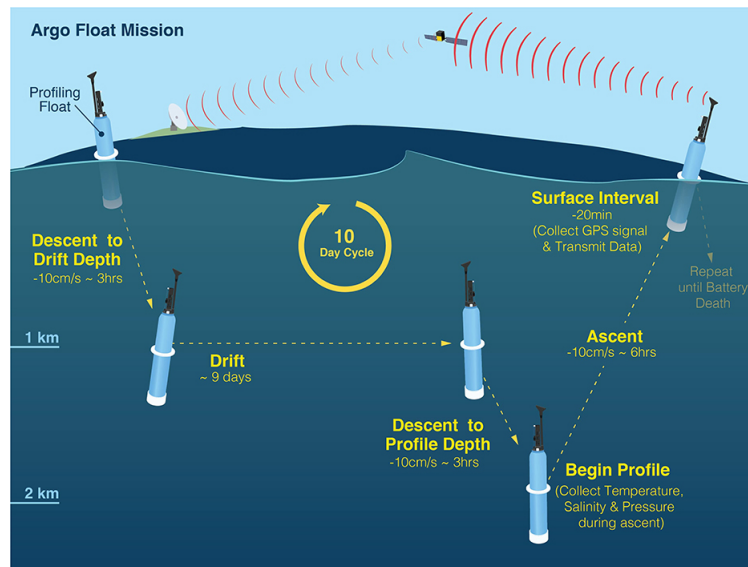


Figure 1: Illustration of the standard Argo “park-and-profile” mission. Source: (Wong et al., 2020)

1.1 Spatial Interpolation of Argo Data

Spatially continuous maps of temperature and salinity measurements are essential to multidisciplinary scientific research. However, despite the planetary scale and subsurface reach of the Argo profiling network, not all locations are sampled. Since other ocean variables depend heavily on temperature and salinity, efforts are focused on obtaining the best interpolated maps of these two variables. Several institutions have produced high-resolution gridded global temperature and salinity datasets from the sparse measurements recorded by the Argo profiling floats using various interpolation techniques (Liu et al., 2020). The list includes the EN4 dataset from the U.K. Met Office (Good et al., 2013) and the grid point value of the monthly objective analysis using Argo data (MOAA) of the Japan Agency for Marine-Earth Science and Technology (JAMSTEC) (Hosoda et al., 2008), both of which use various optimal interpolation methods and covariance functions. Another example is the Barnes objective analysis Argo (BOA-Argo) gridded dataset that employs objective interpolation based on Barnes successive correction method (Li et al., 2017).

One of the most highly used Argo data product is the Roemmich–Gilson Argo climatology

from the Scripps Institution of Oceanography (Roemmich and Gilson, 2009). They used weighted local regression in its high-resolution global mapping. Suppose $\mathbf{s} = (L, l, p)^\top$ is the spatial location vector and t is time in yeardays. For $\mathbf{s}_0 = (L_0, l_0, p_0)^\top$, a reference spatial location vector, and t_0 , the reference time index, they fit the mean function:

$$\begin{aligned} \mu_{\mathbf{s}_0, t_0}(\mathbf{s}, t) = & \beta_0 + \beta_1(L - L_0) + \beta_2(l - l_0) + \beta_3(L - L_0)^2 + \beta_4(l - l_0)^2 + \beta_5(p - p_0) + \beta_6(p - p_0)^2 \\ & + \sum_{k=1}^6 \gamma_k \sin\left(2\pi k \frac{t}{365.25}\right) + \sum_{k=1}^6 \delta_k \cos\left(2\pi k \frac{t}{365.25}\right) \end{aligned} \quad (1)$$

to measurements from the sampled location (L, l, p) , such that (L, l) is one of the 100 nearest neighbor from (L_0, l_0) , for t within 12 calendar months from t_0 , and for p which is one pressure level above and below p_0 . Here β_0 and β_k , γ_k , and δ_k , $k = 1, \dots, 6$, are scalar coefficients. Furthermore, they modelled the residuals using the spatial covariance function:

$$C(L_1, L_2; l_1, l_2) \propto 0.77 \exp\left[-\left\{\frac{h_{\text{RG}}(L_1, L_2; l_1, l_2)}{140 \text{ km}}\right\}^2\right] + 0.23 \exp\left\{-\frac{h_{\text{RG}}(L_1, L_2; l_1, l_2)}{1111 \text{ km}}\right\}, \quad (2)$$

where $h_{\text{RG}}(L_1, L_2; l_1, l_2)$ is a distance function of the form:

$$h_{\text{RG}}(L_1, L_2; l_1, l_2) = \sqrt{(L_1 - L_2)^2 + (l_1 - l_2)^2 + \text{penalty}(L_1, L_2; l_1, l_2)^2}.$$

Kuusela and Stein (2018) improved the modelling of the residuals by using an anisotropic exponential space-time covariance function, i.e.,

$$C(L_1, L_2; l_1, l_2; t_1, t_2) = \sigma^2 \exp\{-h_{\text{KS}}(L_1, L_2; l_1, l_2; t_1, t_2)\}, \quad (3)$$

where $\sigma^2 > 0$ is a variance parameter and $h_{\text{KS}}(L_1, L_2; l_1, l_2; t_1, t_2)$ is a new distance function that captures anisotropy, i.e.,

$$h_{\text{KS}}(L_1, L_2; l_1, l_2; t_1, t_2) = \sqrt{\left(\frac{L_1 - L_2}{\theta_{\text{lat}}}\right)^2 + \left(\frac{l_1 - l_2}{\theta_{\text{lon}}}\right)^2 + \left(\frac{t_1 - t_2}{\theta_t}\right)^2}.$$

Here $\theta_{\text{lat}} > 0$, $\theta_{\text{lon}} > 0$, and $\theta_t > 0$ are range parameters for the latitude, longitude, and time

dimensions, respectively.

Previous studies begin with discretizing the vertical domain of the Argo data into distinct pressure levels and performing the high resolution spatial interpolation of each layer separately. Furthermore, prior to fitting their proposed means and covariance functions, given the irregular sampling of Argo profiles along pressure, a linear interpolation is done to obtain measurements at the fixed pressure levels. This extra step can significantly introduce errors to the model. To address this problem, Yarger et al. (2022) proposed treating the Argo profile data as a functional data that changes with pressure and introduced a functional model for the mean of the form:

$$\begin{aligned} \mu_{L_0, l_0, t_0}(L, l, p, t, y) = & \sum_{\tilde{y}=2007}^{2016} \beta_{0, \tilde{y}}(p) \mathbb{1}_{(y=\tilde{y})} + \beta_1(p)(L - L_0) + \beta_2(p)(l - l_0) \\ & + \beta_3(p)(L - L_0)^2 + \beta_4(p)(l - l_0)^2 + \beta_5(p - p_0) + \beta_6(p - p_0)^2 \\ & + \sum_{k=1}^6 \gamma_k \sin\left(2\pi k \frac{t}{365.25}\right) + \sum_{k=1}^6 \gamma_k \cos\left(2\pi k \frac{t}{365.25}\right). \end{aligned} \quad (4)$$

Here y denotes the year the measurement was obtained, $\mathbb{1}_{(\cdot)}$ is an indicator function, and $\beta_{0,y}(p)$ and $\beta_k(p)$, $k = 1, \dots, 6$, are functions that direct how the coefficients change along pressure. Similar to the mean function in (1), the functional mean (4) is fitted to the measurements from the nearest neighbors. This functional data approach reports lower prediction errors than the pressure-by-pressure approach. The residuals from Yarger et al. (2022) were then modelled using functional principal components.

The aforementioned studies and other results in the Argo literature typically model temperature separately from salinity rather than leverage joint information that may be contained by the two variables. In this work, we extend the spatial modelling of temperature and salinity residuals to include their joint spatial dependence structures. Furthermore, we propose bivariate spatial models in 3D space that can incorporate special oceanographic structures. The ocean, as a fluid, has a density which is a continuous function of depth or pressure. This density dictates the layering of the ocean waters or ocean stratification which is a phenomenon that occurs when different types of water meet and mix, e.g. low-temperature and low-salinity subarctic

water, high-temperature and high-salinity subtropical water, and other mixtures (Sambe and Suga, 2022). Because temperature and salinity exist within this fluid, the ocean stratification can affect their distributions. Bivariate spatial models that account for the ocean structure in the vertical dimension certainly will provide a better description of the processes involved.

The rest of the paper is structured as follows: Section 2 describes the data used for the analysis and provides various empirical analyses. Section 3 introduces the models for the 3D bivariate spatial modelling. Section 4 presents the results of model fitting and prediction. Section 5 concludes.

2 Background

We aim to uncover the spatial relationship lingering among the temperature and salinity residuals obtained by Yarger et al. (2022) so that a clear understanding regarding the dynamics between temperature and salinity can be made. Accomplishing such task can enable one to visualize the vertical structure of the ocean that is not directly observable and to exploit their spatial relationship for prediction at locations with no measurements.

Figures 2 and 3 show the temperature and salinity residuals, respectively, at the surface for the first quarter of every year from 2007 to 2016. There does not jump out any striking pattern of spatial dependence apart from that the values of the residuals near the equator and the coasts are significantly different from their respective neighbors. This hints to weak spatial dependence in those regions. Moreover, there are regions on the open seas where the residual at any one location look similar to its neighbors, i.e., the green spot stretches across a wide area. This signifies that the spatial dependence is strong in those regions. Apart from these observations, no other remarkable features are detected.

More complex patterns can be revealed as we dive below the surface. Suppose \tilde{D} is the area

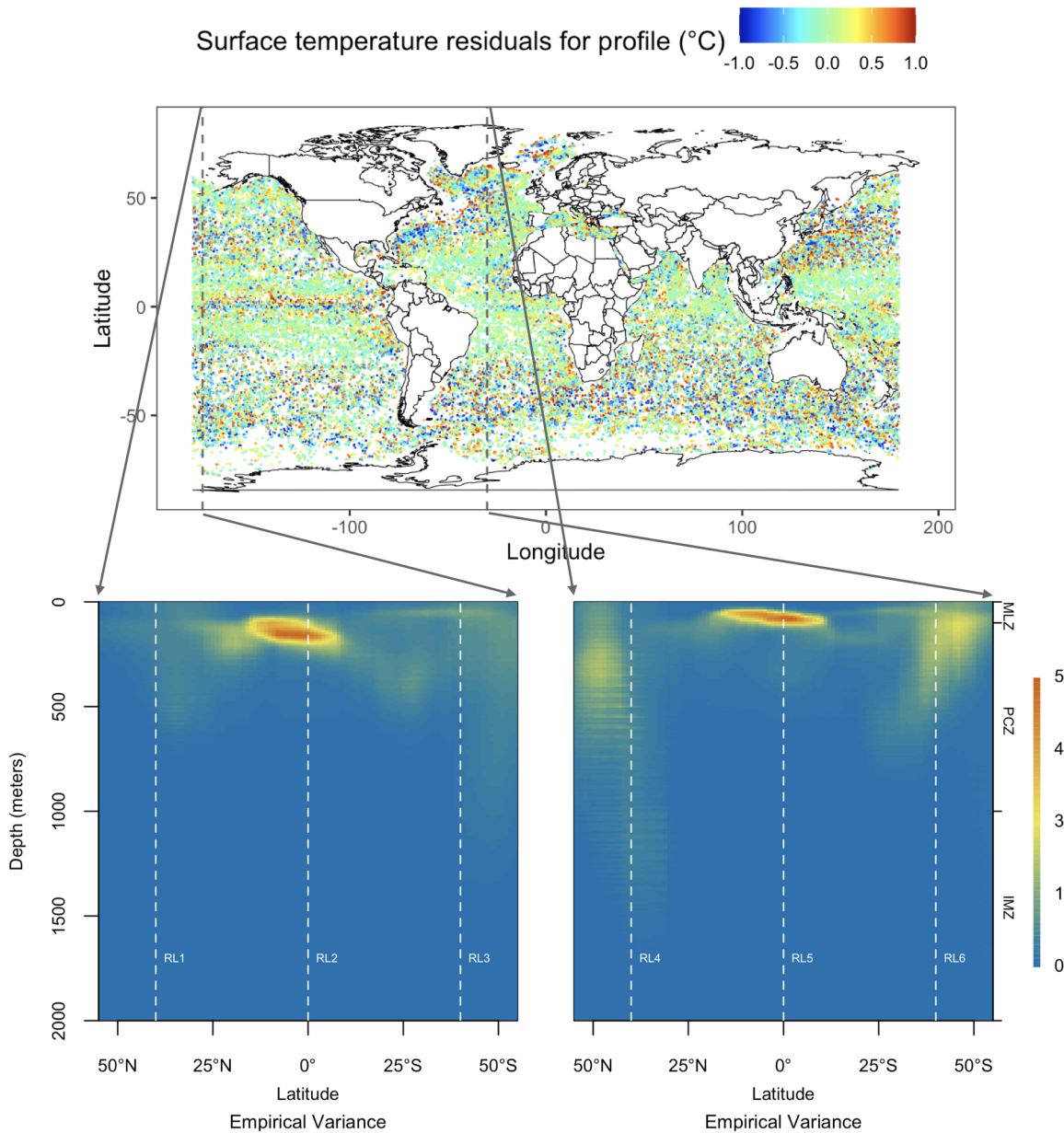


Figure 2: (Top) Temperature residuals from January to March in years 2007 to 2016 obtained by Yarger et al. (2022) is plotted. (Bottom) Empirical variances at every 10 meter depth interval along the two longitude lines are displayed. These longitudes were particularly chosen so that no land forms are crossed going from the topmost latitude down to the bottommost latitude and a full vertical map of empirical variances and correlations of the ocean variables can be produced. We marked 6 reference locations, namely $(40^{\circ}N, 175^{\circ}W)$, $(0^{\circ}, 175^{\circ}W)$, $(40^{\circ}S, 175^{\circ}W)$, $(40^{\circ}N, 30^{\circ}W)$, $(0^{\circ}, 30^{\circ}W)$, and $(40^{\circ}S, 30^{\circ}W)$, for subsequent analyses. The boundaries of the ocean stratification are also indicated as MLZ for mixed layer zone at 0-100 meters depth, PCZ for pycnocline zone at 100-1000 meters depth, and IMZ for intermediate zone at 1000-2000 meters depth. Note that pressure measured in dbar and the depth in meters are approximately equal, i.e., 1 dbar is approximately 1 meter depth. Thus, pressure and depth are used interchangeably throughout this work.

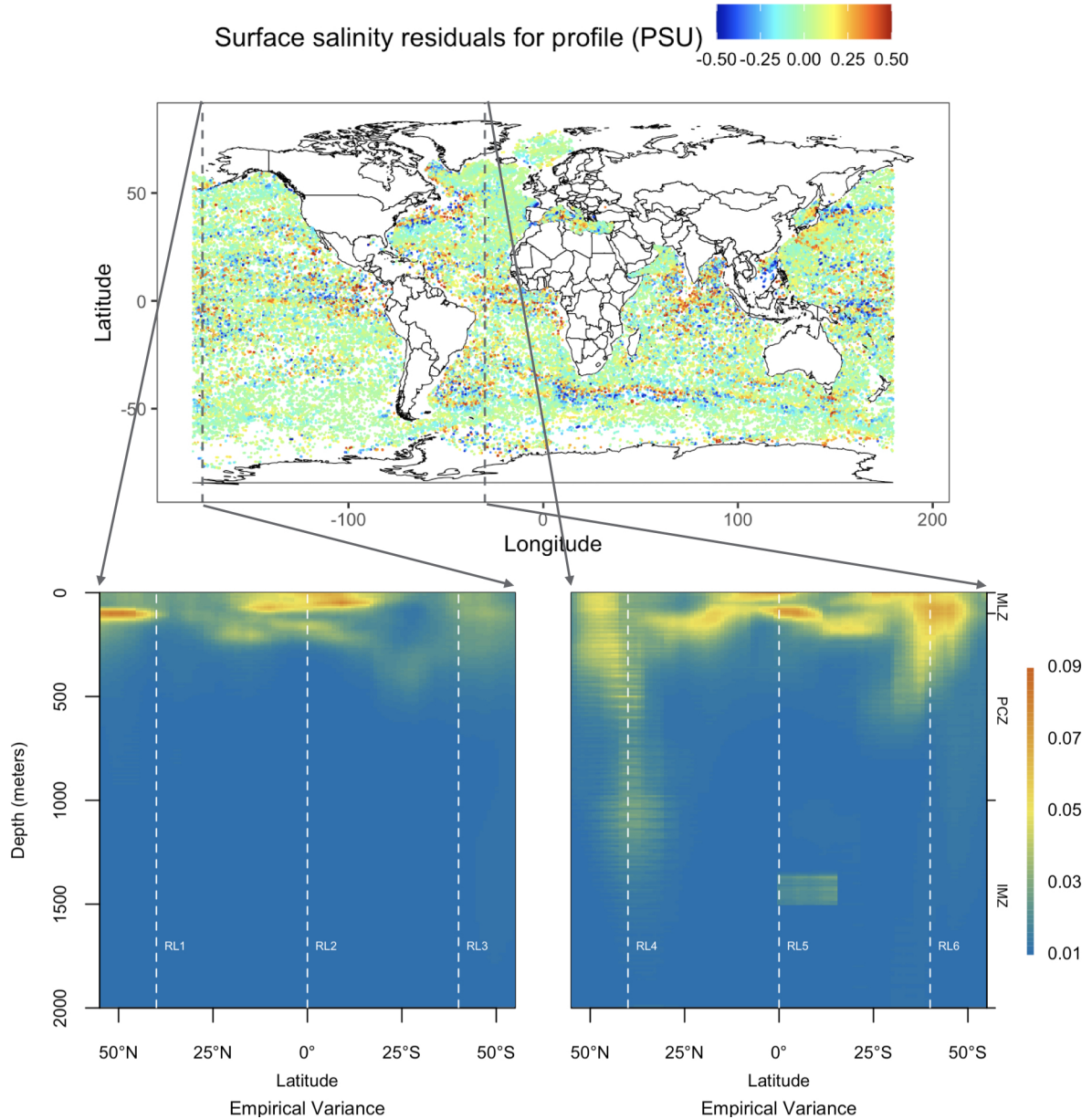


Figure 3: (Top) Salinity residuals from January to March in years 2007 to 2016 obtained by Yarger et al. (2022). (Bottom) Empirical variances at every 10 meter depth interval along the two longitude lines are displayed.

surrounding a reference location \mathbf{s} . Using the following formulas:

$$\hat{\sigma}_X^2(\mathbf{s}) = \frac{\sum_{\tilde{\mathbf{s}} \in \tilde{\mathcal{D}}} \{X(\tilde{\mathbf{s}}) - \bar{\mu}_X(\mathbf{s})\}^2}{|\tilde{\mathcal{D}}|} \quad \text{and} \quad \hat{\rho}_{TS}(\mathbf{s}) = \frac{\sum_{\tilde{\mathbf{s}} \in \tilde{\mathcal{D}}} \{T(\tilde{\mathbf{s}}) - \bar{\mu}_T(\mathbf{s})\} \{S(\tilde{\mathbf{s}}) - \bar{\mu}_S(\mathbf{s})\} / |\tilde{\mathcal{D}}|}{\hat{\sigma}_T(\mathbf{s}) \hat{\sigma}_S(\mathbf{s})},$$

we compute for the empirical variances and colocated correlation between temperature and salinity, respectively, at every location along the $175^\circ W$ and $30^\circ W$ longitude lines at a $1^\circ \times 1^\circ \times$

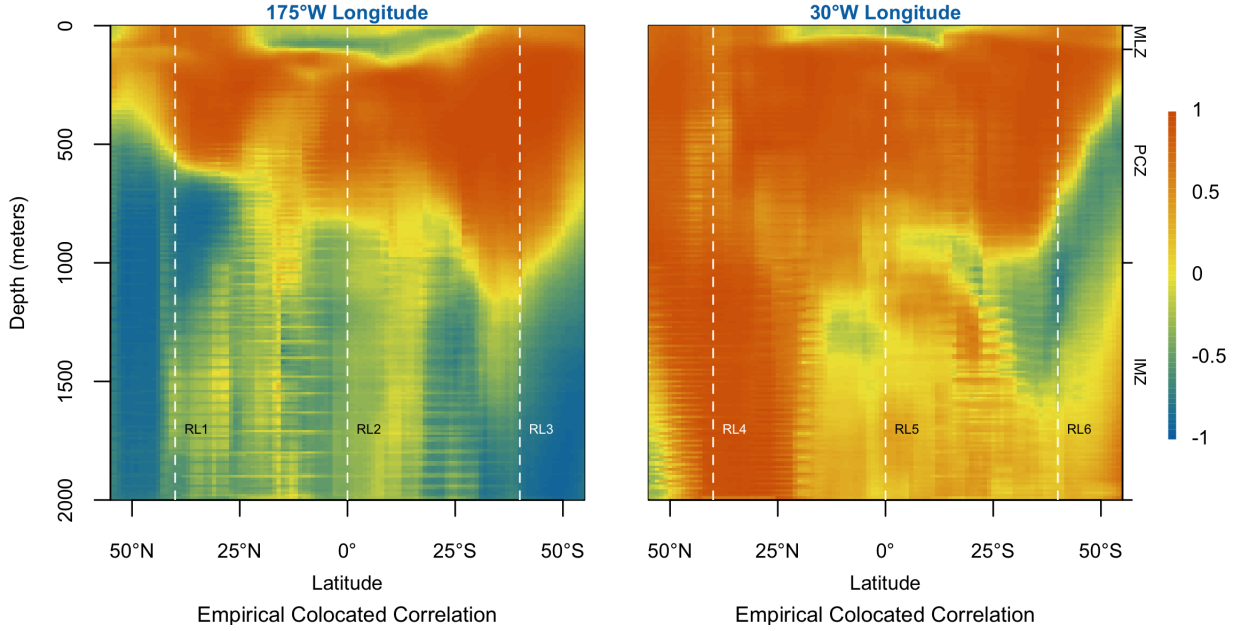


Figure 4: Empirical colocated correlation computed using temperate and salinity residuals from January to March in years 2007 to 2016.

10 meters horizontal and vertical resolution. Here $\hat{\sigma}_X^2(\mathbf{s})$ is the empirical variance of variable X at location \mathbf{s} , where $X = \{T, S\}$ for temperature and salinity, respectively, $\hat{\rho}_{TS}(\mathbf{s})$ is the correlation between temperature and salinity measured at the same location \mathbf{s} , and $\bar{\mu}_X(\mathbf{s})$ is the empirical mean of X at \mathbf{s} such that $\bar{\mu}_X(\mathbf{s}) = \sum_{\tilde{\mathbf{s}} \in \tilde{\mathcal{D}}} X(\tilde{\mathbf{s}})/|\tilde{\mathcal{D}}|$. Computing these values requires measurements of X at location $\tilde{\mathbf{s}}$, where $\tilde{\mathbf{s}}$ is any location inside the domain $\tilde{\mathcal{D}}$, which contains $|\tilde{\mathcal{D}}|$ number of locations. In this work, $\tilde{\mathcal{D}}$ is chosen to be a vertical cylinder with a radius of 900 km and a height of 10 meters centered at \mathbf{s} . Below the surface maps of Figures 2 and 3, the values of the empirical variances are displayed as heatmaps. Figure 4 shows the heatmap of the empirical colocated correlations.

Figures 2 and 3 reveal that the empirical variances change with depth. It can be seen that, in general, there is more variability with the residuals towards the surface which decreases as the depth or pressure increases. Moreover, there are certain depths where the empirical variances drop sharply, which happens at about the 200 to 300 meters mark. Furthermore, the maximum variances are also attained at that region. These results are in agreement with previous findings in the literature (McPhaden and Hayes, 1991; Xie et al., 2000; Chen and Wang, 2016; Chen

et al., 2018; Al Senafi and Anis, 2020). These patterns are justified when considering the three principal horizontal depth zones of the ocean based on density, namely, the surface layer or mixed layer zone (MLZ), the pycnocline zone (PCZ), and the intermediate zone (IMZ) or the deep layer (Chen and Geng, 2019). The surface layer is the topmost layer which stretches, on average, up to 100 meters down and is directly heated by the sun. This layer is where the winds, waves, and currents occur such that their interaction allows for the homogeneous dispersion of heat throughout its depth. The turbulent mixing happening in this region produces uniform vertical structure of temperature and salinity measurements, hence, the variances at this zone are generally not as high as those seen in the next zone (Helber et al., 2012; Maes and O’Kane, 2014). The pycnocline is the region where density changes drastically with depth. This layer is an invisible blanket that separates the warmer and less dense surface layer above and colder and denser deep layer below. This region coincides with the thermocline, the region of sudden decrease in temperature, and with the halocline, the region of sudden increase in salinity. A salient feature of this zone is that it is where the highest variances appear. This is because most eddies are trapped in this particular region which introduce chaotic structures (Dong et al., 2014; Chen and Wang, 2016; Chen et al., 2018). Past the pycnocline is the intermediate zone or the deep layer, a region most isolated from the atmosphere. In this layer, the temperature and salinity values are fairly uniform which explains the sustained small variances from the boundary of the pycnocline.

Figure 4 provides valuable insights on how the two processes interact. Generally, temperature decreases with pressure while salinity increases with pressure. However, this relationship does not directly translate to the observed correlations. From the plot, it can be seen that within a thin region at the surface, temperature and salinity are generally independent, with correlation more or less equal to zero. As they approach the pycnocline, they become highly positively correlated with peaks recorded at the depths of 200 to 500 meters. Beyond the pycnocline, along the $175^{\circ}W$ longitude, the correlation drops again as pressure increases until temperature and

salinity become highly negatively correlated. This behavior of peak correlation at the pycnocline was also observed in Chen and Geng (2019). According to the authors, this pattern is not surprising as the climatological patterns of temperature and salinity are homogeneous around this area. As a result, this layer is also called the “temperature and salinity mirror layer”. A similar pattern is not followed by the locations along the $30^\circ W$ longitude where high positive correlations can persist from the surface to 2000 meters down. This sustained intense correlation can be explained by the dynamic process called meridional overturning circulation which is strongly experienced in the Atlantic Ocean crossed by the $30^\circ W$ longitude (Chen and Geng, 2019). A process called density compensation allows for this temperature-salinity relationship to hold in this area.

3 Methodology

In the previous section, it was shown that the variances and colocated correlation of the residuals change with depth and the vertical structure at one location may not be representative of the other locations. For such phenomenon, spatial nonstationary cross-covariance functions defined in 3D space ought to be used to model the second-order structure of the residuals. We now build 3D spatial models that can accommodate the aforementioned spatially varying features, namely, the variances and colocated correlations, that are present in the Argo residuals.

3.1 Multivariate Nonstationary Spatial Models in 3D domain

We treat temperature and salinity residuals as variables of two different 3D (latitude \times longitude \times depth (i.e., pressure)) processes with zero mean that may or may not be correlated and encode the information regarding their spatial dependence structure in a spatial nonstationary cross-covariance function, denoted $C_{ij}(\mathbf{s}_1, \mathbf{s}_2)$, where $C_{ij}(\mathbf{s}_1, \mathbf{s}_2) = \text{cov} \{Z_i(\mathbf{s}_1), Z_j(\mathbf{s}_2)\}$, $i, j = 1, 2$, such that $Z_1 = T$ and $Z_2 = S$. Here $Z_i(\mathbf{s}_1)$ is the value of variable i at location \mathbf{s}_1 and $Z_j(\mathbf{s}_2)$ is the value of variable j at location \mathbf{s}_2 . Only functions that verify the well-known requirement of

positive definiteness can be considered valid models for C_{ij} .

The literature is replete with cross-covariance function models. The parsimonious Matérn cross covariance function proposed by Gneiting et al. (2010) is one of the most popular models through which more sophisticated models are built upon. It has proposed the form:

$$C_{ij}(\mathbf{s}_1, \mathbf{s}_2) = \frac{\rho_{ij}\sigma_i\sigma_j}{2^{\nu_{ij}-1}\Gamma(\nu_{ij})} \mathcal{M}_{\nu_{ij}} \{h(\mathbf{s}_1, \mathbf{s}_2)\}, \quad (5)$$

for $i, j = 1, \dots, q$, where $h(\mathbf{s}_1, \mathbf{s}_2)$ is a distance function evaluated at locations \mathbf{s}_1 and \mathbf{s}_2 , $\mathcal{M}_\nu(x) = x^\nu \mathcal{K}_\nu(x)$, $\mathcal{K}_\nu(\cdot)$ is the modified Bessel function of the second kind of order ν , $\Gamma(\cdot)$ is the gamma function, and q is the number of variables. Here the parameter list includes, for $i = j$, the marginal variance ($\sigma_i^2 > 0$), and smoothness ($\nu_{ii} > 0$) parameters, and for $i \neq j$, the collocated correlation (ρ_{ij}) and cross smoothness ($\nu_{ij} > 0$) parameters, such that $\nu_{ij} = \frac{1}{2}(\nu_{ii} + \nu_{jj})$ and

$$\rho_{ij} = \beta_{ij} \frac{\Gamma(\nu_{ii} + \frac{d}{2})^{1/2} \Gamma(\nu_{jj} + \frac{d}{2})^{1/2}}{\Gamma(\nu_{ii})^{1/2} \Gamma(\nu_{jj})^{1/2}} \frac{\Gamma(\nu_{ij})}{\Gamma(\nu_{ij} + \frac{d}{2})}, \quad (6)$$

for any $\sigma_{ii}^2, \nu_{ii} > 0, d \geq 1$. Here $(\beta_{ij})_{i,j=1}^q$ is a symmetric and positive definite correlation matrix. For 3D processes on a globe such that $\mathbf{s} = (L, l, p)^\top$ represents the latitude, longitude, and pressure, the following function can be used:

$$h(L_1, L_2, l_1 - l_2, p_1 - p_2) = a_h^2 \text{ch}^2(L_1, L_2, l_1 - l_2) + a_v^2 (p_1 - p_2)^2, \quad (7)$$

where a_h and a_v are the scale parameters in the horizontal and vertical directions, respectively, and $\text{ch}(L_1, L_2, l_1 - l_2)$ is the chordal distance given by the formula:

$$\text{ch}(L_1, L_2, l_1 - l_2) = 2R \left\{ \sin^2 \left(\frac{L_1 - L_2}{2} \right) + \cos L_1 \cos L_2 \sin^2 \left(\frac{l_1 - l_2}{2} \right) \right\}^{1/2}. \quad (8)$$

Here R is the radius of the sphere. For global processes such as the ocean temperature and salinity, the sphere is the Earth with $R = 6,371$ km.

The Matérn cross-covariance function in (5) with distance function in (7) is nonstationary with respect to the latitude but stationary with respect to longitude and pressure. Moreover,

the model is stationary with respect to its parameters such that the variances, σ_i^2 , colocated correlations, ρ_{ij} , and the scale parameters, a_h and a_v , are kept constant everywhere in the sphere, for $i, j = 1, \dots, q$. Kleiber and Nychka (2012) proposed a nonstationary extension to the parsimonious Matérn cross-covariance function (5) in 2D (latitude \times longitude) such that the variances and scales can vary in space, i.e.,

$$C_{ij}(\mathbf{s}_1, \mathbf{s}_2) = \rho_{ij} \sigma_i(\mathbf{s}_1) \sigma_j(\mathbf{s}_2) \mathcal{M}_{\nu_{ij}} \left\{ (\mathbf{s}_1 - \mathbf{s}_2)^\top \mathbf{D}_{ij}(\mathbf{s}_1, \mathbf{s}_2)^{-1} (\mathbf{s}_1 - \mathbf{s}_2) \right\}, \quad (9)$$

where $\mathbf{D}_{ij}(\mathbf{s}) = \frac{1}{2} \{ \mathbf{D}_i(\mathbf{s}_1) + \mathbf{D}_j(\mathbf{s}_2) \}$ is a $d \times d$ positive definite kernel matrix which controls the spatially varying anisotropy, for $i, j = 1, \dots, q$. Despite these innovations, a valid extension of (5) with nonstationary colocated correlation parameter, $\rho_{ij}(\mathbf{s})$, remains elusive. Turns out, the task of generalizing ρ_{ij} to change with location is not trivial. One way to introduce nonstationarity to ρ_{ij} is to replace β_{ij} in (6) with a kernel smoothed nonparametric estimator, $\beta_{ij}(\mathbf{s}_1, \mathbf{s}_2)$, as suggested by Kleiber and Nychka (2012), and in the same principle, σ_i^2 in (5) can be substituted with its kernel smoothed nonparametric estimator using the following formulas:

$$\begin{aligned} \hat{\sigma}_i^2(\mathbf{s}) &= \frac{\sum_{\tilde{\mathbf{s}} \in \tilde{\mathcal{D}}} K_{\lambda_h, \lambda_v}(\mathbf{s}, \tilde{\mathbf{s}}) Z_i^2(\tilde{\mathbf{s}})}{\sum_{\tilde{\mathbf{s}} \in \tilde{\mathcal{D}}} K_{\lambda_h, \lambda_v}(\mathbf{s}, \tilde{\mathbf{s}})} \quad \text{and} \\ \hat{\beta}_{ij}(\mathbf{s}_1, \mathbf{s}_2) &= \frac{\sum_{\tilde{\mathbf{s}} \in \tilde{\mathcal{D}}} K_{\lambda_h, \lambda_v}(\mathbf{s}_1, \tilde{\mathbf{s}})^{1/2} K_{\lambda_h, \lambda_v}(\mathbf{s}_2, \tilde{\mathbf{s}})^{1/2} Z_i(\tilde{\mathbf{s}}) Z_j(\tilde{\mathbf{s}})}{\hat{\sigma}_i(\mathbf{s}_1) \hat{\sigma}_j(\mathbf{s}_2) \left\{ \sum_{\tilde{\mathbf{s}} \in \tilde{\mathcal{D}}} K_{\lambda_h, \lambda_v}(\mathbf{s}_1, \tilde{\mathbf{s}}) \right\}^{1/2} \left\{ \sum_{\tilde{\mathbf{s}} \in \tilde{\mathcal{D}}} K_{\lambda_h, \lambda_v}(\mathbf{s}_2, \tilde{\mathbf{s}}) \right\}^{1/2}}, \end{aligned} \quad (10)$$

where $K_{\lambda_h, \lambda_v}(\mathbf{s}, \tilde{\mathbf{s}}) = \exp[-\{ \text{ch}^2(L_1, L_2, l_1 - l_2)/\lambda_h + (p_1 - p_2)^2/\lambda_v \}]$ is a nonnegative kernel function with horizontal and vertical bandwidths, λ_h and λ_v , respectively, for $i, j = 1, \dots, q$. This approach, however, does not guarantee that the resulting cross-covariance matrix is positive definite. This issue can be remedied by finding the closest positive definite cross-covariance matrix which is done by setting the negative eigenvalues to a very small positive number. Kleiber and Genton (2013) provided parametric forms of $\beta_{ij}(\mathbf{s}_1, \mathbf{s}_2)$ catering to a specific phenomenon involving minimum and maximum temperature residuals over Colorado which are positively correlated at low elevations and almost independent at high elevations. Their approach hinges on the inclusion of a nugget effect. Moreover, their method is not quite appropriate for usage on

the bivariate Argo dataset because the empirical colocated correlations shown in Figure 4 are not monotonic.

A class of spatial nonstationary cross-covariance functions in 2D using differential operators with respect to latitude and longitude was developed in Jun (2011). The univariate version (in space-time setting) was first developed in Jun and Stein (2007). In their work, the multivariate spatial process can be written in the form:

$$Z_i(L, l) = \sum_{k=1}^K \left\{ a_{i,k}(L) \frac{\partial}{\partial L} + b_{i,k}(L) \frac{\partial}{\partial l} \right\} X_k(L, l) + d_i(L) X_0(L, l), \quad (11)$$

where $X_k(L, l)$, $k = 0 \dots, K$, are independent zero-mean univariate spatial processes, and $a_{i,k}(L)$, $b_{i,k}(L)$, and $d_i(L)$ are non-random functions of the latitude, for $i, j = 1, \dots, q$. The cross-covariance function, i.e., $\text{cov}\{Z_i(L_1, l_1), Z_j(L_2, l_2)\}$ may or may not have a closed form, depending on the form of the univariate spatial covariance function of $X_k(L, l)$. The model in (11) is flexible enough to accommodate negative values in the covariances and to allow for spatially varying colocated correlations.

A restriction inherent in the model above is that the variables, Z_i , $i = 1, \dots, q$, rely on the same $X_k(L, l)$, for any k . The model can be made more flexible by replacing the univariate spatial processes, $X_k(L, l)$, with multivariate spatial processes, $\mathbf{X}_k(L, l) = \{X_{1,k}(L, l), \dots, X_{q,k}(L, l)\}^\top \in \mathbb{R}^q$ such that Z_i do not necessarily depend on the same underlying univariate process but rather on correlated univariate processes. In the following proposition, we propose an extension of (11) with this new innovation and an additional differential operator with respect to pressure:

Proposition 1 *Suppose $\mathbf{X}_k(L, l, p)$, $k = 0 \dots, K$, are independent zero-mean multivariate isotropic spatial processes, such that each $\mathbf{X}_k(L, l, p)$ has q elements with cross-covariance function C_{ij}^0 and $(L, l, p)^\top$ denotes the spatial location in latitude, longitude, and pressure. Define a multivariate process as follows:*

$$Z_i(L, l, p) = \sum_{k=1}^K \left\{ a_{i,k}(L) \frac{\partial}{\partial L} + b_{i,k}(L) \frac{\partial}{\partial l} + c_{i,k}(L, p) \frac{\partial}{\partial p} \right\} X_{i,k}(L, l, p) + d_i(L) X_{i,0}(L, l, p). \quad (12)$$

Furthermore, suppose that the cross-covariance function C_{ij}^0 is chosen to be the parsimonious Matérn cross-covariance function in (5). Then the multivariate process $\mathbf{Z} = (Z_1, Z_2, \dots, Z_q)^\top$ has a matrix-valued nonstationary cross-covariance function

$$C_{ij}(L_1, L_2, l_1 - l_2, p_1, p_2) = K_{ij}^1 \mathcal{M}_{\nu_{ij}-1} \{h(L_1, L_2, l_1 - l_2, p_1 - p_2)^{1/2}\} \\ + K_{ij}^2 \mathcal{M}_{\nu_{ij}} \{h(L_1, L_2, l_1 - l_2, p_1 - p_2)^{1/2}\}, \quad (13)$$

where

$$K_{ij}^1 = \frac{\alpha_{ij}}{4} \sum_{k=1}^K \{a_{i,k}(L_1)a_{j,k}(L_2)h_1h_2 - b_{i,k}(L_1)b_{j,k}(L_2)h_3^2 - c_{i,k}(L_1, p_1)c_{j,k}(L_2, p_2)h_4^2 \\ - a_{i,k}(L_1)b_{j,k}(L_2)h_1h_3 + a_{j,k}(L_2)b_{i,k}(L_2)h_2h_3 - a_{i,k}(L_1)c_{j,k}(L_2, p_2)h_1h_4 \\ + a_{j,k}(L_2)c_{i,k}(L_1, p_1)h_2h_4 - b_{i,k}(L_1)c_{j,k}(L_2, p_2)h_3h_4 - b_{j,k}(L_2)c_{i,k}(L_1, p_1)h_3h_4\} \\ + \alpha_{ij}hd_i(L_1)d_j(L_2), \\ K_{ij}^2 = -\frac{\alpha_{ij}}{2} \sum_{k=1}^K \{a_{i,k}(L_1)a_{j,k}(L_2)h_{12} - b_{i,k}(L_1)b_{j,k}(L_2)h_{33} - c_{i,k}(L_1, p_1)c_{j,k}(L_2, p_2)h_{44} \\ - a_{i,k}(L_1)b_{j,k}(L_2)h_{13} + a_{j,k}(L_2)b_{i,k}(L_1)h_{23}\} + 2\alpha_{ij}\nu_{ij}d_i(L_1)d_j(L_2),$$

and $\alpha_{ij} = \frac{\rho_{ij}\sigma_i\sigma_j}{2^{\nu_{ij}-1}\Gamma(\nu_{ij})}$.

The proof of the proposition is rather straightforward. Refer to Appendix in Jun and Stein (2007) for the exact expressions of h_r and h_{rs} , for $r, s = 1, \dots, 4$.

The new formulation has two main features not present in (11). First, for any k , each $X_{i,k}(L, l, p)$ can have different smoothness, for $i = 1, \dots, q$. Second, the pair, $X_{i,k}(L, l, p)$ and $X_{j,k}(L, l, p)$, for any k , has a colocated correlation ρ_{ij} , that may not be one for $i \neq j$. Note that the model in (11) results in $\rho_{ij} = 1$ for any i, j, k .

Based on the form of the cross-covariance function in (13), it can be seen that nonstationarity can be introduced in the marginal variances, $C_{ii}(L, L, 0, p, p)$, and cross-covariance, $C_{ij}(L, L, 0, p, p)$, along the pressure dimension through the functions $c_{i,k}(L, p)$ and $c_{j,k}(L, p)$. While the parameters $a_{i,k}(L)$ and $b_{i,k}(L)$ introduce asymmetry in the latitude and longitude

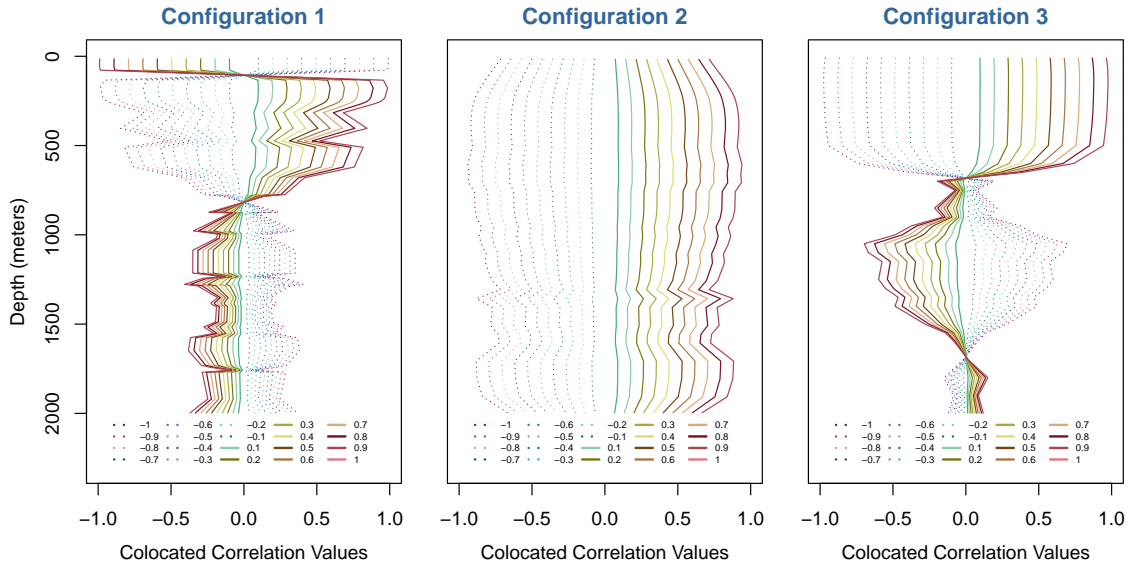


Figure 5: Colocated correlation curves with $\rho_{12} = -1, -0.9, \dots, 0.9, 1$ under different combinations of values for $a_{i,1}(L)$, $b_{i,1}(L)$, $c_{i,1}(L, p)$ and $c_{j,1}(L, p)$, for $i = 1, 2$.

dimensions, respectively, for the field $Z_i(L, l, p)$, and ρ_{ij} is the colocated correlation between $X_{i,k}(L, l, p)$ and $X_{j,k}(L, l, p)$, the effect of their values on the colocated correlation curve, $C_{ij}(L, L, 0, p, p) / \sqrt{C_{ii}(L, L, 0, p, p)C_{jj}(L, L, 0, p, p)}$, of $Z_i(L, l, p)$ and $Z_j(L, l, p)$, cannot be easily distinguished. To facilitate the interpretation of the roles that these parameters play, we plot the values of the colocated correlation curve using different values of ρ_{ij} under three configurations. Suppose $q = 2$, $K = 1$, and $d_{1,1} = d_{2,1} = 0$. Configuration 1 refers to the values of $a_{i,1}(L)$, $b_{i,1}(L)$, $c_{i,1}(L, p)$ and $c_{j,1}(L, p)$, for $i = 1, 2$, such that we are able to replicate the colocated correlation curve at RL2 in Figure 4, when $\rho_{12} = 1$. Similarly, Configurations 2 and 3 refer to the sets of parameter values that result to the colocated correlation curves at RL4 and RL6 in Figure 4, respectively, when $\rho_{12} = 1$. Figure 5 shows the corresponding colocated correlation curves. From the plots, it can be seen that the values of $a_{i,1}(L)$, $b_{i,1}(L)$, $c_{i,1}(L, p)$, and $c_{j,1}(L, p)$ influence the shape of the colocated correlation curve. The parameter ρ_{12} , on the other hand, acts like the amplitude of the curve such that it controls the horizontal scaling of the curve.

3.2 Models

We pursue the modelling of the Argo residuals profile by fitting the following seven models with different features and comparing their performances at the six reference locations highlighted in Section 2. Here, the “independent” models allow different marginal structures but the correlation between the two processes (temperature and salinity) is assumed to be zero.

- I1: independent Matérn covariance function with constant variances; see Equation (5) where $\rho_{12} = 0$;
- I2: independent Matérn covariance function with nonparametric spatially varying empirical variances and colocated correlation; see Equation (5) where σ_1^2 and σ_2^2 are replaced with $\hat{\sigma}_1^2(\mathbf{s})$ and $\hat{\sigma}_2^2(\mathbf{s})$ in (10) and $\rho_{12} = 0$;
- I3: independent differential operator with Matérn covariance function; see Equation (13) where $\rho_{12} = 0$;
- B1: bivariate parsimonious Matérn cross-covariance function with constant variances and colocated correlation parameter; see Equation (5);
- B2: bivariate parsimonious Matérn cross-covariance function with nonparametric spatially varying empirical variances and colocated correlation; see Equation (5) where σ_1^2 , σ_2^2 , and β_{12} are replaced with $\hat{\sigma}_1^2(\mathbf{s})$, $\hat{\sigma}_2^2(\mathbf{s})$, and $\hat{\beta}_{12}(\mathbf{s}_1, \mathbf{s}_2)$ in (10);
- B3: bivariate differential operator with univariate Matérn covariance function; see Equation (13) where $X_{1,k} = X_{2,k}$; and
- B4: bivariate differential operator with bivariate parsimonious Matérn cross-covariance function; see Equation (13).

Table 1 summarizes the models and their properties. Some remarks regarding the configurations of the models:

- a) In a preliminary analysis, a full version of I1 was fitted to all six reference locations and the results show that the effective smoothness for temperature and salinity in those regions are equal to 1. Hence, we fix the effective smoothness for both variables in all the models to 1.

Table 1: Summary of model properties and number of parameters.

Model	Properties	No. of Parameters
I1	parametric, stationary, independent	4
I2	semi-parametric, nonstationary, independent	2
I3	parametric, nonstationary, independent	# of knots for Temperature & Salinity + 4
B1	parametric, stationary, bivariate	5
B2	semi-parametric, nonstationary, bivariate	2
B3	parametric, nonstationary, bivariate	# of knots for Temperature & Salinity + 4
B4	parametric, nonstationary, bivariate	# of knots for Temperature & Salinity + 5

- b) Modelling is done locally as we operate under the assumption of local stationarity in the horizontal dimension. Hence, for I3, B3, and B4, the coefficients $a_{i,k}$ and $b_{i,k}$ are assumed constant and, for parsimony, we set $K = 1$ similar to the approach in Jun and Stein (2007).
- c) The full versions of B3 and B4 were examined where $d_{i,1}$, $i = 1, 2$, are also estimated. However, the estimates move toward zero. Hence, the final B3 and B4 under consideration has $d_{i,1} = 0$, for $i = 1, 2$.
- d) To capture the vertical nonstationarity, we model $c_{i,1}(p)$ using B-splines, i.e.,

$$c_{i,1}(p) = \sum_{m=1}^{M_i} \beta_{i,m} B_{i,m}(p), \quad (14)$$

where M is the number of basis functions, $\{B_{i,m}(p)\}_{m=1}^{M_i}$ are the B -spline bases constructed using M_i knots, and $\{\beta_{i,m}\}$ are the corresponding weights of the B -spline bases for variable i . The number of knots are allowed to vary between variables and among the reference locations depending on the observed dependence structure of the data.

- e) Models I2 and B2 may produce a non-positive definite cross-covariance matrix. In such cases, we find the closest positive definite cross-covariance matrix by setting the negative eigenvalues of the cross-covariance matrix to 10^{-17} .

3.3 Estimation Procedure

The nonstationary models I3, B3, and B4 are more versatile but they are more heavily parameterized than the stationary ones. Through $c_{i,1}(p)$, which is parameterized using B-splines, I3, B3, and B4 can capture nonstationary vertical dependence. However, the number and location of the knots of the B-splines will dictate the goodness-of-fit of these models. Using thinly spaced knots is ideal as more detailed nonstationary dependence structure can be captured at small depth intervals. Doing so, however, will increase the dimension of the parameter vector which might cause the estimation routine to run into convergence issues. We address these problems by (I) choosing the optimal set of knots through cross-validation, (II) retrieving reliable initial parameters for the independent model, I3, and (III) using the estimated parameters of I3 as initial parameters for the bivariate models, B3 and B4. For the knot locations, we begin by placing them at the boundaries of the ocean stratification as seen in Figure 2, i.e., at 0, 100, 1000, and 2000 meters. With this preliminary set of knots, we perform the following two-step estimation procedure for I3.

Step 1. Weighted Least Squares Estimation (WLS): Jointly estimate the parameters by minimizing the objective function:

$$\mathcal{Q}(\boldsymbol{\theta}) = \sum_{i,j=1}^2 \sum_{a=1}^n \sum_{b=1}^n \left\{ \hat{C}_{ij}(\mathbf{s}_a, \mathbf{s}_b) - C_{ij}(\mathbf{s}_a, \mathbf{s}_b | \boldsymbol{\theta}) \right\}^2, \quad (15)$$

where $\boldsymbol{\theta}$ is a vector of parameters and $\hat{C}_{ij}(\mathbf{s}_a, \mathbf{s}_b)$ is the kernel smoothed empirical cross-covariance computed from the data as follows:

$$\hat{C}_{ij}(\mathbf{s}_1, \mathbf{s}_2) = \frac{\sum_{\tilde{\mathbf{s}} \in \tilde{\mathcal{D}}} K_{\lambda_h, \lambda_v}(\mathbf{s}_1, \tilde{\mathbf{s}})^{1/2} K_{\lambda_h, \lambda_v}(\mathbf{s}_2, \tilde{\mathbf{s}})^{1/2} Z_i(\tilde{\mathbf{s}}) Z_j(\tilde{\mathbf{s}})}{\left\{ \sum_{\tilde{\mathbf{s}} \in \tilde{\mathcal{D}}} K_{\lambda_h, \lambda_v}(\mathbf{s}_1, \tilde{\mathbf{s}}) \right\}^{1/2} \left\{ \sum_{\tilde{\mathbf{s}} \in \tilde{\mathcal{D}}} K_{\lambda_h, \lambda_v}(\mathbf{s}_2, \tilde{\mathbf{s}}) \right\}^{1/2}}. \quad (16)$$

Step 2. Maximum Likelihood Estimation (MLE): Jointly estimate the parameters, with the WLS estimates from Step 1 as initial values, by maximizing the Gaussian log-likelihood func-

tion:

$$l(\boldsymbol{\theta}) = -\frac{nq}{2} \log(2\pi) - \frac{1}{2} \log |\boldsymbol{\Sigma}(\boldsymbol{\theta})| - \frac{1}{2} \mathbf{Z}^\top \boldsymbol{\Sigma}(\boldsymbol{\theta})^{-1} \mathbf{Z}, \quad (17)$$

where $\mathbf{Z} = \{\mathbf{Z}(\mathbf{s}_1)^\top, \dots, \mathbf{Z}(\mathbf{s}_n)^\top\}^\top$ is the vector of all measurements, $\mathbf{Z}(\mathbf{s}) = \{T(\mathbf{s}), S(\mathbf{s})\}$, and $\boldsymbol{\Sigma}(\boldsymbol{\theta})$ is the $nq \times nq$ cross-covariance matrix for \mathbf{Z} with determinant $|\boldsymbol{\Sigma}(\boldsymbol{\theta})|$.

The above model fitting procedure can be repeated with a different set of knots such that new knots are added at the midpoints of the previous set of knots until the value of $l(\boldsymbol{\theta})$ for I3 does not significantly improve anymore. Once the MLE estimates of I3 are obtained, we perform the MLE of B3 and B4 with the MLE estimates of I3 as initial values. Note that B3 has the same set of parameters as I3, however, B4 has one additional parameter, ρ_{12} , initialized at zero. The aforementioned fitting procedure is aligned with the overall motivation of this paper, that is, to show whether bivariate modelling can improve upon modelling the variables independently.

Despite employing a local stationary framework, the size of the Argo residuals dataset can render the operations involved for MLE computationally infeasible. Inverting the covariance matrix requires $\mathcal{O}(n^2q^2)$ memory complexity and $\mathcal{O}(n^3q^3)$ computation complexity. On average, a 900 km radius around a reference location contains 2,000 Argo profiles. Furthermore, an Argo profile, on average, has 100 vertical measurements. This translates to a cross-covariance matrix of size $400,000 \times 400,000$. A high performance implementation of the models must be sought when using all those data points. We implement the proposed model on ExaGeoStat (Abdulah et al., 2018), a high performance computing software, to accelerate the operations on the Gaussian log-likelihood function.

4 Results

In this section, we examine the performance of the different candidate spatial covariance functions in modelling the residuals around the six reference locations. Each reference location exhibits a particular vertical dependence structure which some models may be able to represent better than the others. We measure and compare the performances in terms of how well the model

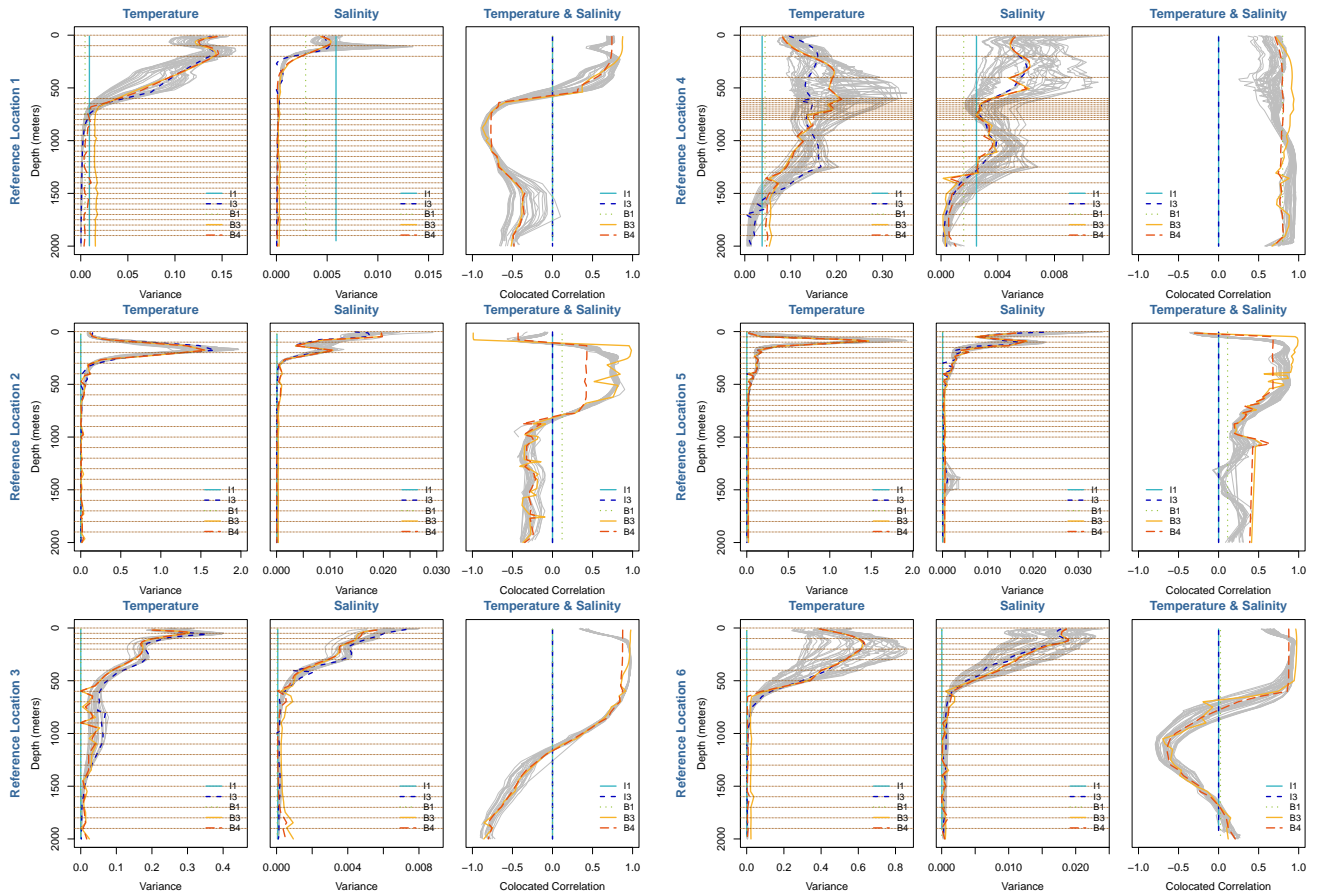


Figure 6: The nonparametric estimators of the empirical marginal variances and colocated correlations (gray) of Argo floats around different reference locations are plotted as a function of depth or pressure alongside the corresponding estimates. Note that the gray curves are used in models I2 and B2.

can explain the observed residuals using the log-likelihood function values and how well the model can predict unobserved residuals using the mean square error (MSE) values. To penalize model complexity, the corresponding Akaike information criterion (AIC) is also computed. For prediction purposes, the Argo float closest to the reference location mark is removed and not included in the model fitting. Table 2 reports the aforementioned values.

From the log-likelihood values, the bivariate models have better performances than their independent counterparts. The most flexible model that best explain the 3D bivariate dependence structure between temperature and salinity residuals appears to be B4. The log-likelihood value of B4 at all six reference locations is the highest among the seven models. Furthermore, as I3 is

Table 2: Modelling and prediction performances of the seven models at six reference locations. The higher the log-likelihood (Log-Lik) value, the better. The opposite is true for the rest. The best scores are highlighted in bold.

Reference Location	Model	Log-Lik ($\times 10^4$)	AIC ($\times 10^5$)	MSE	
				Temperature	Salinity
RL1	I1	8,868	-1,774	0.0699	0.0006
	I2	4,466	-893.0	0.1272	0.0021
	I3	9,200	-1,840	0.0256	0.0003
	B1	8,876	-1,775	0.0628	0.0005
	B2	5,609	-1,122	0.3169	0.1011
	B3	8,701	-1,740	0.0205	0.0005
	B4	9,212	-1,842	0.0252	0.0002
RL2	I1	8,794	-1,759	0.9565	0.0069
	I2	4,536	-908.0	1.9932	0.0261
	I3	9,537	-1,907	1.0857	0.0079
	B1	8,834	-1,767	0.7313	0.0043
	B2	5,477	-1,095	0.6505	0.5039
	B3	9,284	-1,857	0.1988	0.0089
	B4	9,614	-1,923	0.1511	0.0093
RL3	I1	8,906	-1,781	0.2761	0.0055
	I2	3,979	-796.0	0.0911	0.0017
	I3	9,086	-1,817	0.2002	0.0027
	B1	9,148	-1,829	0.0744	0.0015
	B2	5,298	-1,059	0.3699	0.2938
	B3	9,137	-1,827	0.0733	0.0009
	B4	9,198	-1,839	0.3187	0.0100
RL4	I1	7,985	-1,597	6.0361	0.1279
	I2	3,916	-783.0	1.9877	0.0368
	I3	8,431	-1,686	1.7811	0.0279
	B1	8,463	-1,693	0.6599	0.0052
	B2	5,034	-1,007	0.6977	0.2153
	B3	8,134	-1,638	1.0346	0.2220
	B4	8,832	-1,766	0.3399	0.0015
RL5	I1	8,349	-1,669	0.0970	0.0129
	I2	4,660	-932.0	0.2592	0.0104
	I3	8,519	-1,704	0.0991	0.0127
	B1	8,418	-1,684	0.3278	0.0157
	B2	5,454	-1,091	0.1215	0.1051
	B3	8,298	-1,659	1.4413	0.0219
	B4	8,599	-1,719	0.0991	0.0127
RL6	I1	8,305	-1,661	0.8429	0.0603
	I2	1,714	-343.0	0.9156	0.0646
	I3	8,456	-1,691	0.9400	0.0672
	B1	8,523	-1,705	0.0436	0.0233
	B2	4,186	-837.2	0.1408	0.0617
	B3	8,762	-1,752	0.0211	0.0035
	B4	8,871	-1,774	0.0209	0.0033

Table 3: Parameter estimates associated with the differential operators in the horizontal dimension for models I3, B3, and B4. The values for \hat{a}_1 , \hat{b}_1 , \hat{a}_2 , and \hat{b}_2 are in 10^{-6} . Note that only $\hat{\rho}_{12}$ of B4 was estimated.

Reference Location	Model	$\hat{\rho}_{12}$	\hat{a}_1	\hat{b}_1	\hat{a}_2	\hat{b}_2	range (km)		distance (km) of prediction float to the nearest float
							horizontal	vertical	
RL1	I3	0	61.64	-68.21	27.21	-13.94			
	B3	1	6,757	-5,356	-256.9	1,005	70.09	0.0866	25.19
	B4	0.77	3,626	438.9	-603.2	-78.71			
RL2	I3	0	0.242	-0.174	0.012	-0.049			
	B3	1	45.57	6.162	-0.599	-4.376	23.00	0.0491	3.29
	B4	0.43	12.81	-8.349	-0.445	1.886			
RL3	I3	0	16.79	-0.286	36.63	7.549			
	B3	1	336.6	26.01	3.176	1.497	175.9	0.0276	34.13
	B4	0.88	224.5	113.2	3.929	2.081			
RL4	I3	0	1,423	17.11	190.8	0.937			
	B3	1	10,151	-8,467	455.7	-112.7	278.8	0.1006	61.60
	B4	0.81	6,937	929.3	1,093	172.5			
RL5	I3	0	1.416	-0.163	5×10^{-6}	-0.472			
	B3	1	64.85	-14.36	11.36	-18.75	180.4	0.0287	46.42
	B4	0.68	12.05	-59.80	3.956	-18.19			
RL6	I3	0	7×10^{-7}	0.545	0.124	0.469			
	B3	1	11.32	16.67	-16.64	-1.255	207.9	0.0593	27.72
	B4	0.88	9.768	14.96	-13.79	-4.282			

an independent nested version of B4, the performance of B4 is always better than I3. However, this is not what is always seen between the I3 and B3 modelling performances. In RL1, RL2, RL4, and RL5, the independent model, I3, has higher log-likelihood values than the bivariate model, B3. This is because I3 is not nested under B3. Due to its formulation, the estimation of B3 effectively starts with a fixed parameter $\rho_{12} = 1$, while B4 starts with $\rho_{12} = 0$. The restrictive form of B3 does not allow for the cross-covariance structure to deviate away from the marginal covariance structures. This is where the utility of Proposition 1 appears. The additional parameter ρ_{12} in B4 allows the other parameters to adjust in order to capture the true underlying cross-covariance structure. In Table 3, we summarized the estimated parameter values associated with the differential operators in the horizontal dimension. For brevity, we omit the presentation of the parameters associated with $c_i(p)$. That the parameters of B4 deviate from its simpler counterpart, B3, suggests that B3 is way too restrictive as a bivariate model. Figure 6 displays the fitted variances and colocated correlation values by the different models.

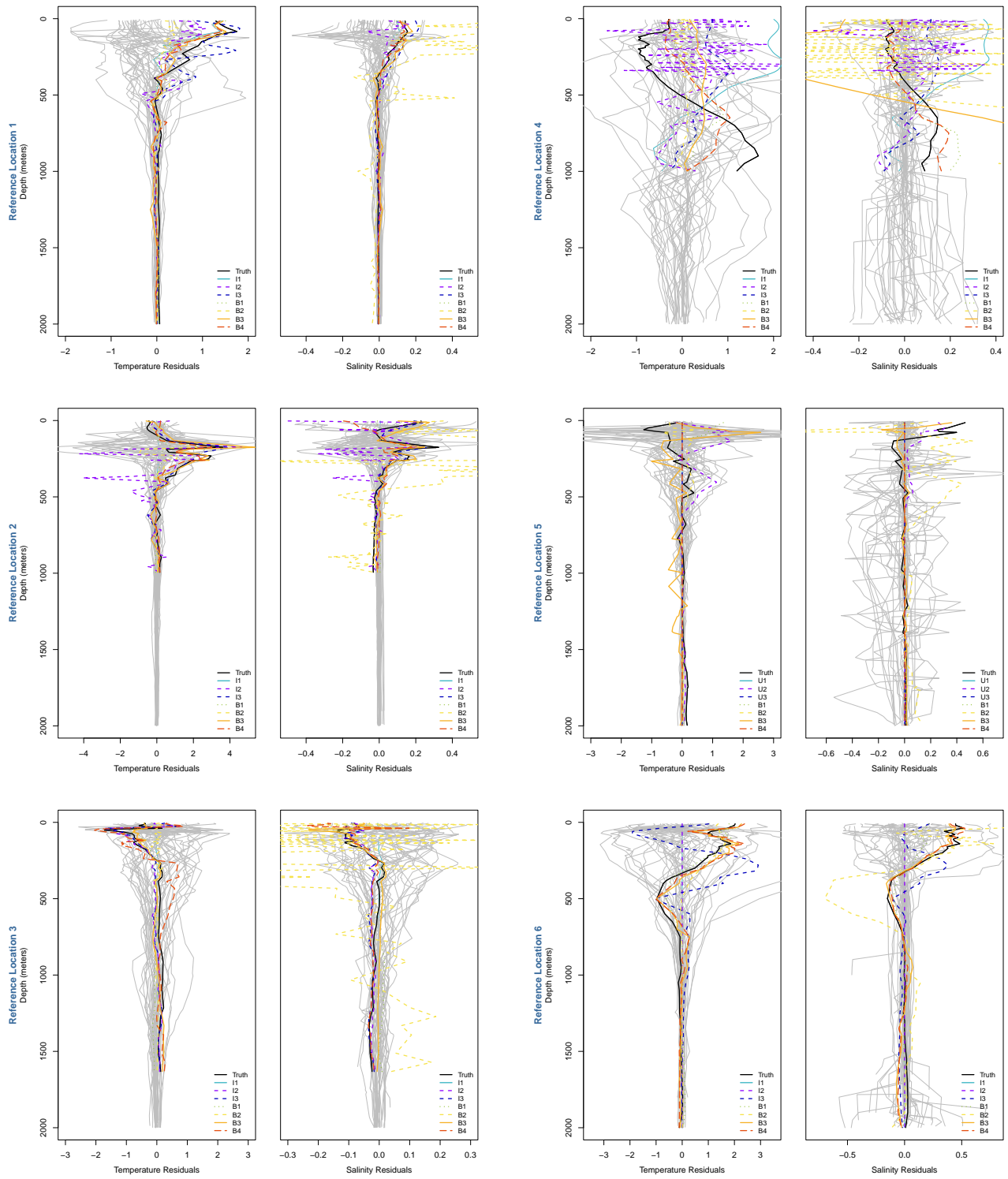


Figure 7: The predictions by each model for the Argo float situated nearest the reference location (black) are drawn. The other Argo residuals profile in the region are also overlaid in gray for reference.

To illustrate the benefits of having a secondary variable to aid the prediction of a primary variable, we perform prediction on one variable at a time. When predicting the temperature (salinity) residuals at the Argo float which was left out for prediction, we use the temperature and salinity residuals included in modelling fitting plus the salinity (temperature) residuals at the same Argo float which was left out for prediction. While the interpretation of the results for the modelling as expressed by the log-likelihood and AIC criteria is straightforward, the prediction metric MSE does not point to one obvious winner. Except at RL5, the bivariate models report lower MSEs compared to the independent models. This demonstrates the utility of having another correlated variable present to aid prediction. To improve the prediction at RL5, we may need to prescribe a more sophisticated form for $c_i(p)$ and the cross-covariance parameters may need to be set independently from the marginals. The prediction performances at RL5 reveal the importance of correctly modelling the colocated correlation. Because we assume that we have the measurements of the secondary variable at the same location where we aim to predict the main variable, the models generally give more weight on the colocated secondary variable compared to the values of the other neighboring Argo floats. Thus, underestimating or overestimating this colocated correlation may lead to erroneous predictions.

5 Concluding Remarks

Argo floats play an important role in sampling the temperature and salinity measurements of the world's oceans. Despite the global reach of the Argo network of floats, not all locations are sampled. We contributed to the efforts of producing high quality temperature and salinity interpolations at unsampled locations through a bivariate modelling of the Argo residuals. Motivated by the interesting physical dynamics between temperature and salinity, we took the modelling one step further by incorporating the vertical properties of the ocean. Consistent with previous studies, we illustrated that the correlation between temperature and salinity changes with depth and successfully modelled this vertical dependence structure using a nonstationary cross-

covariance function. Our proposed model is flexible enough to accommodate different vertical oceanographic regions. This study provides a framework to improve mapping of environmental variables in 3D. Further work may be pursued such as constructing new models that allow the cross-covariance parameters to be set independently from the marginals and the range parameters to change with depth. Furthermore, a 4D modelling may also be explored with time as an additional dimension.

References

- Abdulah, S., Ltaief, H., Sun, Y., Genton, M. G., and Keyes, D. E. (2018). ExaGeoStat: A high performance unified software for geostatistics on manycore systems. *IEEE Transactions on Parallel and Distributed Systems*, 29(12):2771–2784.
- Al Senafi, F. and Anis, A. (2020). Internal waves on the continental shelf of the Northwestern Arabian Gulf. *Frontiers in Marine Science*, page 805.
- Argo, G. (2000). Argo float data and metadata from global data assembly centre (Argo GDAC). *Seanoë*.
- Chen, G. and Geng, D. (2019). A “mirror layer” of temperature and salinity in the ocean. *Climate Dynamics*, 52(1):1–13.
- Chen, G., Peng, L., and Ma, C. (2018). Climatology and seasonality of upper ocean salinity: a three-dimensional view from Argo floats. *Climate Dynamics*, 50(5):2169–2182.
- Chen, G. and Wang, X. (2016). Vertical structure of upper-ocean seasonality: Annual and semiannual cycles with oceanographic implications. *Journal of Climate*, 29(1):37–59.
- Chen, L., Zhang, R.-H., and Gao, C. (2022). Effects of temperature and salinity on surface currents in the Equatorial Pacific. *Journal of Geophysical Research: Oceans*, 127(4):e2021JC018175.
- Ding, D.-S., Patel, A. K., Singhanian, R. R., Chen, C.-W., and Dong, C.-D. (2022). Effects of temperature and salinity on growth, metabolism and digestive enzymes synthesis of goniopora columna. *Biology*, 11(3):436.
- Dong, C., McWilliams, J. C., Liu, Y., and Chen, D. (2014). Global heat and salt transports by eddy movement. *Nature Communications*, 5(1):1–6.
- Escobar, A., Negro, V., López-Gutiérrez, J. S., and Esteban, M. (2016). Influence of temperature and salinity on hydrodynamic forces. *Journal of Ocean Engineering and Science*, 1(4):325–336.

- Galán, A., Saldías, G. S., Corredor-Acosta, A., Muñoz, R., Lara, C., and Iriarte, J. L. (2021). Argo float reveals biogeochemical characteristics along the freshwater gradient off western patagonia. *Frontiers in Marine Science*, 8:613265.
- Gangopadhyay, A. (2022). *Introduction to Ocean Circulation and Modeling*. CRC Press.
- Gneiting, T., Kleiber, W., and Schlather, M. (2010). Matérn cross-covariance functions for multivariate random fields. *Journal of the American Statistical Association*, 105(491):1167–1177.
- Good, S. A., Martin, M. J., and Rayner, N. A. (2013). En4: Quality controlled ocean temperature and salinity profiles and monthly objective analyses with uncertainty estimates. *Journal of Geophysical Research: Oceans*, 118(12):6704–6716.
- Helber, R. W., Kara, A. B., Richman, J. G., Carnes, M. R., Barron, C. N., Hurlburt, H. E., and Boyer, T. (2012). Temperature versus salinity gradients below the ocean mixed layer. *Journal of Geophysical Research: Oceans*, 117(C5).
- Hosoda, S., Ohira, T., and Nakamura, T. (2008). A monthly mean dataset of global oceanic temperature and salinity derived from Argo float observations. *JAMSTEC Report of Research and Development*, 8:47–59.
- Hu, A. J., Kuusela, M., Lee, A. B., Giglio, D., and Wood, K. M. (2020). Spatio-temporal methods for estimating subsurface ocean thermal response to tropical cyclones. *arXiv preprint arXiv:2012.15130*.
- Jana, S., Gangopadhyay, A., Haley, P. J., and Lermusiaux, P. F. (2022). Sound speed variability over Bay of Bengal from Argo observations (2011-2020). In *OCEANS 2022-Chennai*, pages 1–8. IEEE.
- Johnson, G. C., Hosoda, S., Jayne, S. R., Oke, P. R., Riser, S. C., Roemmich, D., Suga, T., Thierry, V., Wijffels, S. E., and Xu, J. (2022). Argo-two decades: global oceanography, revolutionized. *Annual Review of Marine Science*, 14:379–403.
- Jun, M. (2011). Non-stationary cross-covariance models for multivariate processes on a globe. *Scandinavian Journal of Statistics*, 38(4):726–747.
- Jun, M. and Stein, M. L. (2007). An approach to producing space–time covariance functions on spheres. *Technometrics*, 49(4):468–479.
- Kleiber, W. and Genton, M. G. (2013). Spatially varying cross-correlation coefficients in the presence of nugget effects. *Biometrika*, 100(1):213–220.
- Kleiber, W. and Nychka, D. (2012). Nonstationary modeling for multivariate spatial processes. *Journal of Multivariate Analysis*, 112:76–91.

- Kuusela, M. and Stein, M. L. (2018). Locally stationary spatio-temporal interpolation of Argo profiling float data. *Proceedings of the Royal Society A*, 474(2220):20180400.
- Li, H., Xu, F., Zhou, W., Wang, D., Wright, J. S., Liu, Z., and Lin, Y. (2017). Development of a global gridded Argo data set with Barnes successive corrections. *Journal of Geophysical Research: Oceans*, 122(2):866–889.
- Liu, C., Liang, X., Chambers, D. P., and Ponte, R. M. (2020). Global patterns of spatial and temporal variability in salinity from multiple gridded Argo products. *Journal of Climate*, 33(20):8751–8766.
- Maes, C. and O’Kane, T. J. (2014). Seasonal variations of the upper ocean salinity stratification in the tropics. *Journal of Geophysical Research: Oceans*, 119(3):1706–1722.
- McPhaden, M. J. and Hayes, S. P. (1991). On the variability of winds, sea surface temperature, and surface layer heat content in the western equatorial Pacific. *Journal of Geophysical Research: Oceans*, 96(S01):3331–3342.
- Olson, S., Jansen, M. F., Abbot, D. S., Halevy, I., and Goldblatt, C. (2022). The effect of ocean salinity on climate and its implications for Earth’s habitability. *Geophysical Research Letters*, 49(10):e2021GL095748.
- Pawlowicz, R. (2013). Key physical variables in the ocean: temperature, salinity, and density. *Nature Education Knowledge*, 4(4):13.
- Roemmich, D. and Gilson, J. (2009). The 2004–2008 mean and annual cycle of temperature, salinity, and steric height in the global ocean from the Argo program. *Progress in Oceanography*, 52(2):81–100.
- Sambe, F. and Suga, T. (2022). Unsupervised clustering of Argo temperature and salinity profiles in the mid-latitude Northwest Pacific Ocean and revealed influence of the Kuroshio extension variability on the vertical structure distribution. *Journal of Geophysical Research: Oceans*, 127(3):e2021JC018138.
- Walker, R. H., Smith, G. D., Hudson, S. B., French, S. S., and Walters, A. W. (2020). Warmer temperatures interact with salinity to weaken physiological facilitation to stress in freshwater fishes. *Conservation Physiology*, 8(1):coaa107.
- Wong, A. P., Wijffels, S. E., Riser, S. C., Pouliquen, S., Hosoda, S., Roemmich, D., Gilson, J., Johnson, G. C., Martini, K., Murphy, D. J., et al. (2020). Argo data 1999–2019: two million temperature-salinity profiles and subsurface velocity observations from a global array of profiling floats. *Frontiers in Marine Science*, page 700.

- Xie, S.-P., Kunitani, T., Kubokawa, A., Nonaka, M., and Hosoda, S. (2000). Interdecadal thermocline variability in the North Pacific for 1958–97: A GCM simulation. *Journal of Physical Oceanography*, 30(11):2798–2813.
- Yarger, D., Stoev, S., and Hsing, T. (2022). A functional-data approach to the Argo data. *The Annals of Applied Statistics*, 16(1):216–246.